RSC Advances

PAPER

Cite this: *RSC Adv.*, 2014, **4**, 26993

Successful aqueous processing of a lead free $0.5Ba(Zr_{0.2}Ti_{0.8})O_3–0.5(Ba_{0.7}Ca_{0.3})TiO_3$ piezoelectric material composition

Ajay Kaushal,*[a] S. M. Olhero,[a] Budhendra Singh,[b] Reza Zamiri,[a] V. Saravanan†[a] and J. M. F. Ferreira*[a]

Received 8th April 2014
Accepted 28th May 2014

DOI: 10.1039/c4ra03172e

www.rsc.org/advances

We report on the successful aqueous processing of a lead free piezoelectric $0.5Ba(Zr_{0.2}Ti_{0.8})O_3$ $0.5(Ba_{0.7}Ca_{0.3})TiO_3$ (BZT BCT) composition with the final functional properties of the materials unaffected by the various processing steps involved. X-ray diffraction results show a single tetragonal perovskite crystalline phase for the as-received sintered BZT BCT powder. The purity of the perovskite phase for BZT BCT powder was found to be controlled even after ageing the material in water for 24 h as a successful surface treatment against hydrolysis. An aqueous suspension of surface treated BZT BCT powder with 50 vol% solid loading was successfully transformed into micro-sized granules *via* a freeze granulation (FG) method. Various structural, electrical and mechanical properties of sintered BZT BCT-FG and BZT BCT-NG ceramics consolidated from freeze granulated and non-granulated (NG) powders, respectively, were measured. The dielectric constant (ε_r) values of the BZT BCT-FG sample were found to be higher, with lower dielectric loss (tan δ) values in comparison with those of a sample prepared from the BZT BCT-NG powder at all temperatures and with all frequency ranges tested. Nanoindentation results revealed that the ability to oppose deformation was nearly 10-fold higher for BZT BCT-FG (6.93 GPa) than for BZT BCT-NG ceramics (543 MPa). The functional properties of BZT BCT-FG samples confirmed the benefits of the aqueous processing approach in comparison with traditional dry pressing.

A Introduction

Successful aqueous processing of multicomponent electroceramics relies on their various functional properties being unaffected by the chance of there being ionic leaching in water.[1,2] $0.5Ba(Zr_{0.2}Ti_{0.8})O_3–0.5(Ba_{0.7}Ca_{0.3})TiO_3$ (BZT–BCT) has been reported as an interesting lead free ferroelectric system that exhibits the highest piezoelectric coefficient $d_{33} \sim 620$ pC N^{-1} and is a good candidate material to replace lead-based Pb $[Zr_xTi_{1-x}]O_3$ (PZT) piezoelectric ceramics.[3–5] BZT–BCT is a representative dielectric material with a high dielectric constant for multilayer ceramic capacitor applications.[6,7] There have been recent reports in the literature on the sintering behavior of BZT–BCT material showing dielectric properties at various sintering temperatures.[8–11] Depending on a material's functional applications, it is necessary to control its structural and compositional evolution to achieve superior properties. Furthermore, the materials need to be consolidated in bulk (polycrystalline ceramics, single crystals) or in film (thick and thin) form to draw benefits from their relevant properties. A reduction in dimension of all passive components without compromising performance, and improved reliability are desirable in electronics technology.

To date, non-aqueous processing of electroceramics is preferred because of the common water sensitiveness of the starting powders and the consequent leaching of material components, which affects the final product functional properties and often results in exaggerated grain growth and low final density.[12,13] The reason for the detrimental effects of water is believed to be the instability of alkaline-earth titanates in water, which were first observed experimentally in calcium titanate ($CaTiO_3$).[14] However, aqueous processing is attractive from both environmental and economical standpoints. The knowledge acquired with aqueous processing of other water sensitive powders such as magnesium aluminate ($MgAl_2O_4$) and zirconia-toughened-alumina (ZTA)[15,16] is likely to be helpful here, and the recently demonstrated feasibility of aqueous processing of BZT–BCT electroceramic powders[17] could be regarded as an aid to designing the necessary experiments aimed at preparation of high performance granulated powders

[a]*Department of Materials and Ceramic Engineering, CICECO, University of Aveiro, 3810 193, Aveiro, Portugal. E mail: ajay.kaushal@ua.pt; jmf@ua.pt; Fax: +351 234 370204; Tel: +351 234 370354*

[b]*Department of Mechanical Engineering and TEMA, University of Aveiro, 3810 193, Aveiro, Portugal*

† Present address: Department of Physics, School of Basic and Applied Sciences, Central University of Tamil Nadu, Thiruvarur 610101, India.

for dry pressing. Relevant aspects include the surface chemistry of the particles and how to control this through the selection of type and amount of dispersant, and the rise of pH and concentrations of leached ionic species with aging time. Preventing the well-known reactivity of BZT–BCT powders with water is a major challenge towards preparing high-quality spherical granules from aqueous suspensions.[17] Therefore, it is essential to investigate how the functional properties of a multicomponent oxide material might be affected by hydrolysis or other steps involved in aqueous processing. When BZT–BCT particles come into contact with water molecules they undergo hydrolysis and, in chemical equilibrium, substantial amounts of Ba^{2+} and Ca^{2+} ions should be leached from BZT–BCT, according to the reaction:

$$\mathrm{BZT} \times \mathrm{BCT} + \mathrm{H_2O} \rightleftharpoons (\mathrm{B}_{1-x_1}\mathrm{ZT} \times \mathrm{B}_{1-x_2}\mathrm{C}_{1-y}\mathrm{T})_{(s)} + (x_1 + x_2)\mathrm{Ba}_{(aq)}{}^{2+} + y\mathrm{Ca}_{(aq)}{}^{2+} + 2(x_1 + x_2 + y)\mathrm{OH}_{(aq)}{}^{-} \quad (1)$$

Therefore, protecting BZT–BCT powder particles against hydrolysis and hindering the leaching process of alkaline earth ions as described by eqn (1) are important issues,[17] which are extremely relevant for maximizing the performance of BZT–BCT ceramics. The proposed surface treatment, which consists of adding 2 wt% of an aqueous solution of aluminum di-hydrogen phosphate, $Al(H_2PO_4)_3$ (Bindal), proved to be effective in preventing the hydrolysis of BZT–BCT powders. It has been reported that the assembly of Bindal on the surface of the ceramic particles occurs through a chemisorption process of $Al(HPO_4)^{3-}$ or $Al(PO_4)_3{}^{2-}$ species. However, the potential harmful effects of the surface protecting agent, which is likely to contain some aluminum and phosphate species, need to be studied to better support the claim of successful aqueous processing. Earlier findings[17] inspired us to undertake further research aimed at preparing high-quality spherical granules by freeze granulation (FG) from suspensions containing the surface treated powder in the present study, and to assess the potential benefits in terms of the various functional properties of sintered ceramics. The results obtained confirmed that aqueous processing was a viable route to obtain lead free functional ceramics with good, unaffected dielectric properties, provided that the surface of the particles was suitably protected against hydrolysis. The superiority of the aqueous colloidal processing and freeze granulation approach became more evident when the dielectric properties of ceramics derived from FG were compared with those of ceramics derived from non-granulated (NG) powders. This kind of lead free ceramic is desirable for its functional relaxor ferroelectric properties and new processing/sintering approaches are being attempted to improve these compounds in comparison to those prepared by conventional methods.[18]

B Experimental

BZT–BCT powder was synthesized using a conventional solid state reaction from a precursor mixture of high purity $BaCO_3$ (Sigma-Aldrich, Steinheim, Germany), ZrO_2 (Sigma-Aldrich, Steinheim, Germany), TiO_2 (Riedel-de Haen, Sielze, Germany), and $CaCO_3$ (Sigma-Aldrich, Steinheim, Germany). The mixture was firstly dry ball-milled for 1 h, followed by wet ball-milling in ethanol for 2 h to guarantee complete homogenization, and then dried at 100 °C. The dried powder was then calcined at 1000 °C for 4 h, reground by dry ball-milling for 2 h, and then heat treated at 1400 °C for 4 h followed by 1 h dry ball-milling to destroy the coarser agglomerates formed on heat treatments. The as-obtained powder was then attrition milled for 10 h in ethanol at 700 rpm. Aqueous processing of BZT–BCT powder including various steps such as selection of dispersant, ageing effect in water and rheological behavior have been reported elsewhere.[17] The various parameters such as pH *versus* time, different ion concentrations in aqueous solvent, selection of dispersant, dispersant concentration, surface chemical modification and surface ionic charge were monitored to obtain a stable aqueous suspension of BZT–BCT with high solid loadings. To avoid selective ionic leaching, di-hydrogen phosphate was used to protect the powder particles. A BZT–BCT aqueous suspension of 50 vol% solid loading was sprayed into liquid nitrogen (196 °C) to obtain micro-sized granules by freeze granulation (Power Pro freeze granulator LS-2, Gothenburg, Sweden). Duramax B1001 (3 wt%) was added as a binder in the suspension before spraying. The granules were then dried at 49 °C under a pressure of 1×10^{-3} Torr in a freeze-drying system (Lyph-Lock 4.5, Labconco, Kansas City, MO, USA) for 72 h. The dried granules were uniaxial pressed into disc-shaped pellets of 20 mm diameter at a uniaxial pressure of 60 MPa followed by isostatic pressing at 200 MPa aimed at further enhancing the green density of the samples. Finally, after ageing for 24 h in water under constant stirring, samples consolidated from BZT–BCT-FG, BZT–BCT-NG, and centrifuged BZT–BCT powder (BZT–BCT-CF) were sintered at 1350 °C for 4 h.

The flow properties (angle of repose ($\overline{\mathbf{AR}}$), Hausner ratio (HR) and average flow rate (V) through orifice) of FG and NG powders were assessed in batches of 100 g. A Ford cup with a calibrated orifice was fixed 30 cm from a horizontal surface and filled with the powder to be tested. The angle of repose ($\overline{\mathbf{AR}}$) was calculated as:

$$\overline{\mathbf{AR}_n} = \frac{\boldsymbol{\alpha}_1 + \boldsymbol{\alpha}_2}{2}, \quad (2)$$

where: $\boldsymbol{\alpha}_1$ and $\boldsymbol{\alpha}_2$ are the basal angle of the formed pile onto the horizontal surface on two opposed sides, and n is the number of measurements per data point. The average flow rate (V) through the Ford cup orifice was calculated as:

$$\boldsymbol{V}_n = \frac{\boldsymbol{W}_n}{\boldsymbol{T}_n}, \quad (3)$$

where: W is weight measured in a container, at time T, and n is the number of measurements per data point. Five measurements were taken per data point. The HR was also calculated using a graduated measuring cylinder (50 ml, 1 ml accuracy). The volumes of powder samples before (V_1) and after hand tapping until constant volume (V_2) over time were measured to calculate the HR as:

$$\mathrm{HR}_n = \frac{\boldsymbol{V}_{1n}}{\boldsymbol{V}_{2n}}, \quad (4)$$

The crystallinity of the samples was studied using a Rigaku X-ray diffractometer of CuK_α (1.54 Å) radiations in θ–2θ geometry. Pure strain-free silicon was used as an instrumental-standard sample to determine the instrumental broadening effect factor to deduce instrumental inaccuracy in crystallite size calculations from X-ray diffraction (XRD) spectra. Bulk density (ρ_{bulk}) of various sintered BZT–BCT ceramics was measured in ethylene glycol liquid using the Archimedes principle. Three density measurements were performed for each sample. Dilatometry measurements were performed for both FG and NG green compacts using a Dil 801L dilatometer (BAHR-Thermoanalyse). Nanoindentation measurements were performed on a well-polished surface (up to 6 μm diamond suspension) of BZT–BCT ceramic using a three-side pyramidal Berkovich diamond indenter having a nominal edge radius of 120 nm (faces 65.3° from vertical axis) attached to a fully calibrated TTX-NHT nanoindenter (CSM Instruments). The test was carried out under progressive multicycle loading with an acquisition rate of 10 Hz. Load control to various peak loads in the range 20–200 mN with an approach speed of 2000 nm min^{-1} was used. The loading and unloading speed throughout the measurement was kept constant at 30 mN min^{-1}, with a dwell time of 10 s and a pause time of 10 s between each cycle. The microstructure topography of the samples was studied using an S-4100 scanning electron microscopy (SEM; Hitachi, Tokyo, Japan). To prevent charge build-up during SEM observations, samples were coated with carbon. For measurement of electrical properties, sintered samples were polished to a thickness of ~0.35 mm, and top conductive electrodes were deposited on both sides using silver paste. Dielectric constant and loss were measured at different temperatures and frequencies in the ranges of 25–225 °C and 100 Hz–2 MHz, respectively, using a 4294A impedance analyzer (Agilent, USA).

C Results and discussion

C.1 Structural properties

Fig. 1(a) shows SEM images of green BZT–BCT granules obtained after freeze-drying, revealing successful fabrication of spherical shaped micro-sized BZT–BCT granules. This technique involves spraying well-dispersed aqueous suspensions into liquid nitrogen. Quickly freezing the spherical droplets hinders binder segregation and preserves within the granules the high degree of homogeneity achieved in the suspension, in contrast to what happens on spray drying. Furthermore, the granules obtained by FG are massive (not hollow or donut-shaped), softer and less dense, thus being more easily smashed under the applied external pressure and leading to dry powder compacts of high homogeneity.[19] The observed spherical morphology of the granules and their sizes (a few tens of μm) confer to the powder free-flowing ability and a low friction coefficient with the die wall on dry pressing the BZT–BCT compacts.[20] The free-flowing ability is strongly conveyed by the image of BZT–BCT granules (inset in the figure) taken at the edge of the conducting tape. Moreover, the size distribution of the spherical granules was relatively narrow; varying essentially within the range of 25–75 μm. An SEM image of non-granulated BZT–BCT powder after 10 h attrition milling in ethanol is shown in Fig. 1(b). To enable good observation of the separated particles, the starting suspension used to prepare the sample for SEM has to be dilute enough. This is why the SEM micrograph is not particularly crowded with particles. The shape of the particles is relatively isometric and their sizes are distributed according to different populations.

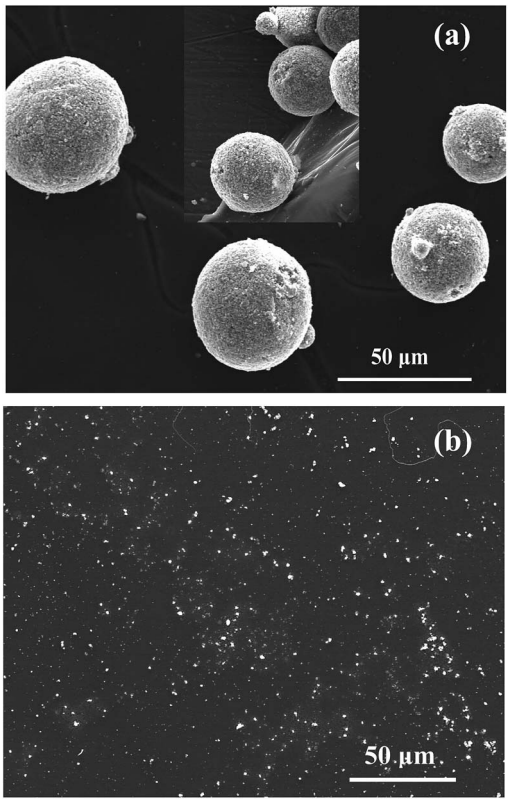

Fig. 1 SEM image of (a) freeze-dried green BZT BCT granules and (b) non granulated BZT BCT powder. Inset in (a) shows free falling view of granules.

Table 1 Various calculated values of $\overline{AR}$, HR and V for FG and NG powders

Powder sample	$\overline{AR}$ (°)	V (g s ^{1})	HR
BZT BCT NG	52 ± 0.5		1.65 ± 0.02
BZT BCT FG	30 ± 1.5	3.5 ± 0.36	1.11 ± 0.01

Free-flowing behavior of FG powder was further confirmed by performing powder rheology for both FG and NG powders. The values of angle of repose ($\overline{AR}$), HR and average flow rate (V) through the orifice calculated from powder rheology tests are listed in Table 1. The results confirmed the excellent flow behavior of the FG powder, which contrasts with that of the NG powder. The average flow rate for FG was found to be $V = 3.5 \pm 0.36$ g s^{-1}, but it could not be determined for NG (the NG powder stacked inside the Ford cup and no flow took place). Therefore, determining the $\overline{AR}$ in this case required mechanically assisted pouring of the NG powder. The $\overline{AR}$ measurements

revealed a lower value for the FG powder ($\overline{\mathbf{AR}} = 30 \pm 1.5°$) in comparison with that of NG powder ($\overline{\mathbf{AR}} = 52 \pm 0.5°$) and the conical pile obtained in this last case was too irregular in shape. The HR was determined using a fixed volume (40 ml) of powders. The HR value measured for FG powder was significantly lower (1.11 ± 0.01) than that obtained for NG powder (1.65 ± 0.02). However, the required weight of FG powder (52.36 ± 0.21 g) was found to be lower when compared with that of NG powder (59.67 ± 0.14 g). These differences reflect the typically lower density of FG spherical granules and their regular sizes, which hinder the interstitial voids being filled with smaller particles, contrasting with the NG powder in which particle rearrangements gradually reduce the apparent volume. The lower density of FG granules can easily be understood considering the absence of capillary forces (shrinkage) during ice sublimation. The same reasons also hinder the segregation of processing additives, making FG powders more homogeneous in comparison to the granules prepared by spray drying. These features are expected to grant uniform mould filling and homogeneous packing of FG powder on dry pressing.

Fig. 2 shows the room temperature XRD pattern of BZT–BCT ceramics sintered at 1350 °C for 4 h, derived from non-granulated powder (BZT–BCT-NG) and before and after aging in water for 24 h (BZT–BCT-CF). It is evident that after solid state reaction and milling the BZT–BCT-NG powder consists of a single tetragonal perovskite phase. The diffraction peaks were indexed to a perovskite-type tetragonal structure with space group (*P4mm*) in agreement with the Joint Committee on Powder Diffraction Standards (JCPDS) card no. 05-0626.[21] However, a completely different result was obtained for BZT–BCT-CF ceramics derived from the same powder but after aging in water for 24 h under constant stirring. In this case, the XRD pattern shows extra impurity phase diffraction peaks together with a pure tetragonal phase. It has been reported that processing of BZT–BCT in aqueous media results in its hydrolysis and non-stoichiometric dissolution reactions, which will alter the composition of the BZT–BCT powder.[17] Therefore, water sensitive particles need to be surface protected against hydrolysis,[15 17] which contrasts with the desired XRD phase purity identified for BZT–BCT-FG ceramics sintered under the same heat treatment schedule, which underwent aqueous processing, as shown in Fig. 2. Close matching to phase structure and the absence of impurity peaks (as depicted from XRD pattern) are observed for both BZT–BCT-NG and BZT–BCT-FG ceramics. This means that the desired purity of the BZT–BCT composition was not altered with colloidal processing in aqueous media when the surface of the particles was protected against hydrolysis. These observations allow us to conclude that no external contamination has been introduced in the preceding processing steps (deagglomeration/milling) in aqueous media. For a deeper analysis, the *a*- and *c*-axis lattice parameters were calculated from the XRD patterns of BZT–BCT-FG and BZT–BCT-NG ceramic samples with tetragonal phase structure.[22] The values of the *a*-axis were found to be 4.001 Å and 4.002 Å for BZT–BCT-NG and BZT–BCT-FG, respectively, whereas the corresponding calculated *c*-axis values were 4.004 Å and 4.006 Å. According to these values, the calculated c/a ratios are 1.0008 and 1.0011 for BZT–BCT-NG and BZT–BCT-FG ceramic materials, respectively. This small difference reveals that the tetragonality of the perovskite structure was not distorted much.

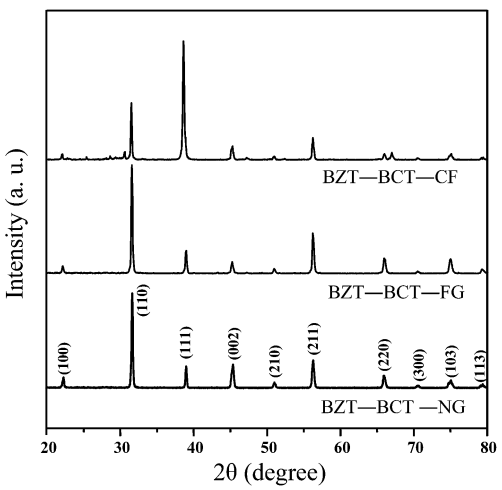

Fig. 2 XRD pattern of BZT BCT-NG, BZT BCT-FG and BZT BCT-CF ceramic samples sintered at 1350 °C for 4 h.

To gain further insight, the crystallite sizes of FG and NG samples were calculated from XRD data using the Williamson–Hall method. The Scherrer equation does not take into account broadening caused by lattice strain present in the sample. Generally, the integral breadth of an XRD peak is given by the integrated intensity divided by the maximum intensity. Thus, the observed peak broadening B_0 may be represented as:

$$\boldsymbol{B_r = B_0 \quad B_i} \tag{5}$$

where: B_0 is the peak broadening observed (in radians), B_i is the instrumental broadening (in radians) and B_r is the broadening caused by the small crystallite size and lattice strain. The instrumental broadening is estimated using a pure strain-free silicon standard subject to XRD under identical conditions. According to the Scherrer equation,[22] the broadening caused by small crystallite size may be expressed as:[23]

$$\boldsymbol{B_c = \frac{k\lambda}{d \cos \theta}} \tag{6}$$

where: B_c is the broadening solely caused by small crystallite size, k is a constant whose value depends on particle shape and is usually taken as unity, d is the crystallite size, θ is the Bragg angle and λ is the wavelength of the incident X-ray beam (1.5418 Å). Similarly, according to Wilson,[24] the broadening caused by lattice strain is expressed as:

$$\boldsymbol{B_s = 4\varepsilon \tan \theta} \tag{7}$$

where: B_s is the peak broadening caused by the lattice strain, ε is the strain distribution within the material and θ is the Bragg angle. Thus the total broadening of the peak is given as the sum of eqn (6) and (7) excluding the instrumental broadening, which can be expressed as:

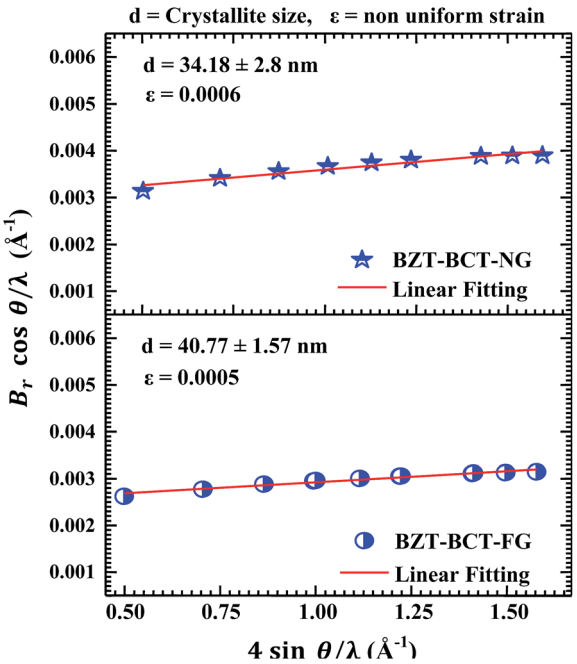

Fig. 3 A typical Hall Williamson plot for BZT BCT-NG and BZT BCT-FG ceramics sintered at 1350 °C for 4 h.

$$B_r = \frac{k\lambda}{d\cos\theta} + 4\varepsilon\tan\theta \quad (8)$$

or

$$\frac{B_r\cos\theta}{\lambda} = \frac{k}{d} + \varepsilon\frac{4\sin\theta}{\lambda} \quad (9)$$

The plot of $(B_r \cos\theta)/\lambda$ *versus* $(4 \sin\theta)/\lambda$ is a straight line with slope equal to ε, and thus, the crystallite size d can be estimated from the intercept. A typical Hall–Williamson plot for BZT–BCT sintered samples when consolidated from NG and FG BZT–BCT powders is shown in Fig. 3. An increase of crystallite size from 34.18 ± 2.8 nm to 40.77 ± 1.57 nm was calculated for sintered BZT–BCT ceramics consolidated from NG and FG BZT–BCT powders, respectively. The observed differences suggest that the diffusion paths have been shortened in the samples derived from the FG powder because of their higher degree of homogenization.[25]

Generally, micron-sized granules obtained by freeze granulation exhibit a number of favorable features in comparison to loose powders or granules obtained by spray drying as follows: (i) lower green density in comparison with granules obtained by spray drying; (ii) are homogeneous (no binder segregation occurs); (iii) free-flowing behavior that enables their spatial rearrangements; and (iv) are easily smashed under the applied pressure. These features favor the elimination of the intergranular pores.[26] The binder in FG granules acts as a lubricant, assisting primary particles sliding and rearranging to increase the packing efficiency and compact density. This explains why the green density of FG compacts is higher in comparison with that of NG compacts (as shown in Table 2). An increase in green density will enhance the densification ability upon sintering, while implying a decrease of total shrinkage. This is confirmed by the data plotted in Fig. 4, which compares the dilatometric curves of FG and NG green bodies measured from room temperature to 1370 °C. It can be seen clearly that the shrinkage starts earlier and progresses at a much faster rate for the FG powder in comparison with the NG one. Essentially, diverging lines that do not deviate much from the horizon can be observed up to ~1100 °C and ~1200 °C for FG and NG samples, respectively. The positive inclination observed for the NG sample reveals that thermal expansion predominates over any shrinkage, while the FG samples exhibit a negative inclination along the lower temperature range, probably because of the homogeneous distribution of the particles and the burnout of binder among them, which allows them to gradually approach each other. The benefits of freeze granulation here are evident, being translated by a downshift of the onset of shrinkage of >100 °C. For the FG sample, the shrinkage becomes very fast for $T \geq$ ~1100 °C, achieving the maximum shrinkage rate at ~1200 °C, whereas the NG sample at a higher temperature (1300 °C) exhibits a shrinkage rate similar to that of the FG sample at 1150 °C. For the FG sample, the maximum density has apparently been achieved at about ~1240 °C with a slope reversion of the dilatometric curve, whereas the densification process of the NG sample was still far from completion at 1370 °C. The dilatometric curves plotted in Fig. 4 are consistent with the results of relative density measured for the sintered samples (Table 2). The highest relative density (96.77 ± 2.29%, based on the density of synthesized BZT–BCT = 5.487 g cm^{-3} measured by helium pycnometry) was obtained for BZT–BCT-FG ceramics, whereas a significantly lower value (93.95 ± 3.45%) was achieved for BZT–BCT-NG ceramics. The

Table 2 Calculated values of densities, linear shrinkage, crystallite sizes and lattice axis parameters for various BZT BCT ceramics sintered at 1350 °C

Samples	ρ_{green} (g cm ^{3})	ρ_{bulk} (g cm ^{3})	$\rho_{relative}$ [a] (%)	Linear shrinkage (%)	*a* axis length (Å)	*c* axis length (Å)	*c*/*a* ratio	Crystallite size (nm)
BZT BCT NG	2.79 ± 0.193	5.155 ± 0.196	93.95 ± 3.45	10.38 ± 0.04	4.001	4.004	1.0008	34.18 ± 2.8
BZT BCT FG	2.87 ± 0.102	5.310 ± 0.126	96.77 ± 2.29	15.21 ± 0.08	4.002	4.006	1.0011	40.77 ± 1.57
BZT BCT CF	2.84 ± 0.183	5.216 ± 0.214	95.06 ± 3.57	12.61 ± 0.02				

[a] Theoretical value of particle density used for relative density calculation was measured to be 5.487 g cm ^{3} using Multi Pycnometer (Quantachrome, USA).

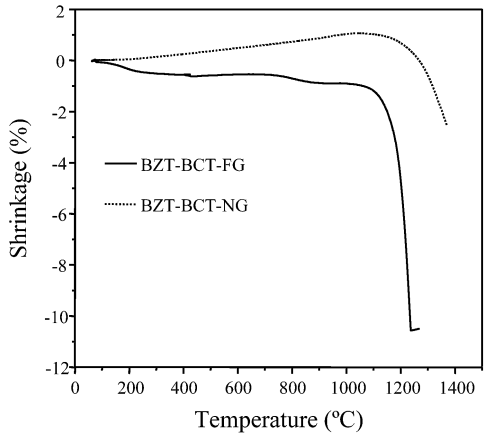

Fig. 4 Dilatometric behavior of BZT BCT-FG and BZT BCT-NG green compacts.

experimental value of powder density (5.487 g cm^{-3}) measured from helium pycnometry was found to be lower than the theoretical density value (5.77 g cm^{-3}) of BZT–BCT powder. The lower measured density could be caused by the effects of 10 h attrition milling on the structure of the outer surface layer of the particles. It is known that severe milling increases lattice stress/strain and often enhances the amorphous fraction.

Fig. 5(a) and (b) shows SEM images of external surfaces of sintered BZT–BCT-NG and BZT–BCT-FG ceramics, respectively. The corresponding images of the surface fractures are shown in Fig. 5(c) and (d). These SEM images reveal different morphological features that reflect the different sintering abilities of BZT–BCT-FG and BZT–BCT-NG powders. Fig. 5(c) clearly shows that the porosity fraction of the BZT–BCT-NG sample is higher than that of the BZT–BCT-FG one, and is in good agreement with the bulk density data determined by the immersion method (Table 2), as well as with the measured geometrical density values, 4.84 ± 0.21 g cm^{-3} and 4.61 ± 0.23 g cm^{-3} for FG and NG ceramics, respectively. The geometrical density values are lower than the corresponding values obtained by the immersion method at 5.310 ± 0.126 g cm^{-3} and 5.155 ± 0.196 g cm^{-3} for FG and NG ceramics, respectively. The differences are attributed to the presence of open pores that increase the apparent volume in the geometrical assessment. Therefore, measuring the sintered density using both methods gives a better idea about the influence of open porosity. It is also clear that the grain size for BZT–BCT-FG ceramics is noticeably larger than that of BZT–BCT-NG ceramics (Fig. 5(c) and (d)).

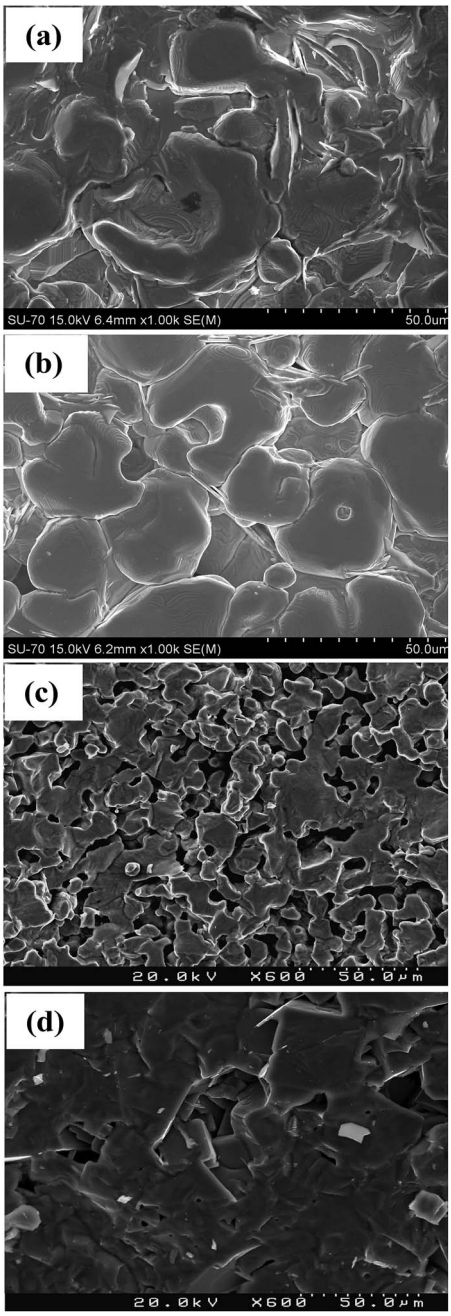

Fig. 5 SEM images of external surfaces of (a) BZT BCT-NG and (b) BZT BCT-FG ceramics sintered at 1350 °C, with corresponding surface fracture images shown in (c) and (d), respectively.

C.2 Hardness

The hardness (H) of the material is defined as the ratio of the peak load, P_{max}, to the projected area under nanoindentation, A_c, *i.e.*,

$$H = P_{max}/A_c, \quad (10)$$

However, the projected area under the nanoindenter depends on the contact depth, h_c, which in turn depends on the shape of the indenter. In the case of the Berkovich nanoindenter (used in the present study), A_c is estimated to be $24.5h_c^2$. Furthermore, according to the Oliver and Pharr analysis,[27] the contact depth can be determined by:

$$h_c = h_{max} \quad 0.75P_{max}/S, \quad (11)$$

where: h_{max} is the displacement at peak load and S is the initial unloading stiffness expressed as dP/dh and can be calculated from the slope of the unloading segment of the load–displacement curve. Seven different imprints were made at various places and aggregated values were used for analysis using the

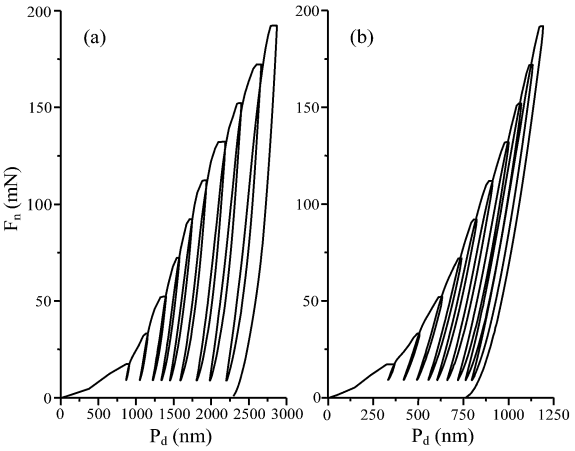

Fig. 6 Load *versus* displacement curve used for (a) BZT BCT-NG and (b) BZT BCT-FG ceramics sintered at 1350 °C.

standard Oliver and Pharr method.[27] Fig. 6(a) and (b) shows a typical load *versus* displacement curve for the BZT–BCT-NG and BZT–BCT-FG ceramics, respectively. Large displacement values were observed for BZT–BCT-NG ceramics when compared with displacement values of BZT–BCT-FG ceramics under application of same load. The lower displacement values observed for the BZT–BCT-FG ceramics reflect the higher stiffness of sintered microstructure derived from compacted freeze granulated powders.

The indentation size, D, which is proportional to the value of contact depth, h_c is related to the peak load as:[28]

$$P = a_0 + a_1 h_c + a_2 h_c^2, \quad (12)$$

where: a_0, a_1 and a_2 are constant parameters. Furthermore, the parameter a_2 is considered to be a measure of the load-independent hardness H_0 and related to the empirical formula given by:[28]

$$H_0 = k a_2, \quad (13)$$

where: k is a constant that depends on the indenter geometry. For a Berkovich indenter, the value of k is 1/24.5. Fig. 7 shows the variation of contact depth h_c with peak load for each indentation cycle. The curve was fitted with a polynomial function (eqn (12)) and the fitted values for a_0, a_1 and a_2 are shown in Table 3. From the best fitting of the experimental results to eqn (12), the calculated ability to oppose deformation for the BZT–BCT-NG ceramics (543 MPa) was found to be nearly 10-fold less than that of BZT–BCT-FG ceramics (6.93 GPa). This significant difference is probably because of the higher number of pores observed in the fracture surface of BZT–BCT-NG ceramic in comparison to that of BZT–BCT-FG. Pores may lead to large displacements of the indenter under the same load.

C.3 Electrical properties

Another aim of the present work was to evaluate if the aqueous processing steps negatively affect the electrical properties of

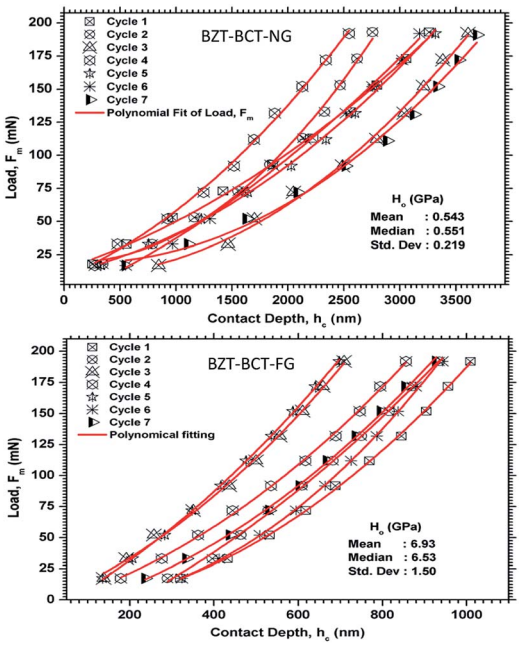

Fig. 7 Variation of contact depth (h_c) with peak load (F_m) along each indentation cycle for BZT BCT-NG and BZT BCT-FG ceramics sintered at 1350 °C.

sintered BZT–BCT-FG in comparison with BZT–BCT-NG ceramics. It was hypothesized that Al and P elements coming from the thermal decomposition of the surface protecting agent $Al(H_2PO_4)_3$ could interfere with the perovskite structure and properties of BZT–BCT.

Fig. 8(a) and (b) shows the temperature dependences of ε_r and tan δ within the range 25–225 °C measured at a constant frequency of 10 kHz. It can be seen that all the ceramics evaluated exhibit a maximum dielectric constant ($\varepsilon_{r_{max}}$) at 95 °C, corresponding to the phase transition temperature (T_c) for $0.5Ba(Zr_{0.2}Ti_{0.8})O_3$–$0.5(Ba_{0.7}Ca_{0.3})TiO_3$ composition (Fig. 8(a)). The corresponding dielectric loss data plotted in Fig. 8(b) reveal maxima values at the proximity of T_c. At T_c, the frequency of the soft mode tends to zero and the lattice displacement associated with it becomes unstable and leads to phase transition.[29] The superiority of aqueous colloidal processing and the freeze granulation approach becomes more evident when the dielectric properties of ceramics derived from FG are compared with those of ceramics derived from NG powders. Two obvious phase transitions above 25 °C corresponding to the orthorhombic–tetragonal and tetragonal–cubic, respectively, were observed for both BZT–BCT-NG and BZT–BCT-FG ceramics.[3] However, BZT–BCT-CF (non-treated powder kept for 24 h in aqueous media under constant stirring) shows significant differences in dielectric response and electrical behavior as only one phase transition was observed for BZT–BCT-CF ceramic, as shown in Fig. 8(a). The absence of phase transition at low temperatures in the case of the BZT–BCT-CF ceramic reflects the chemical phase impurities as a result of hydrolysis (Fig. 2). Furthermore, the value of ε_r at room temperature (30 °C) was found to be higher for BZT–BCT-FG ceramics ($\varepsilon_r \sim 4984$) when compared with

Table 3 Values of various constant parameters calculated from h_c*versus* F_m plot (Fig. 7)

Indentation cycles	BZT BCT NG				BZT BCT FG			
	a_1	a_2	a_3	Adj. R square	a_1	a_2	a_3	Adj. R square
Cycle 1	14.06484	0.02816	7.82315×10^{6}	0.99659	7.04261	0.01898	1.75425×10^{4}	0.99924
Cycle 2	19.56167	0.00313	2.33352×10^{5}	0.99431	33.64236	0.13383	1.15816×10^{4}	0.99855
Cycle 3	9.77102	0.00281	1.46819×10^{5}	0.99442	0.92531	0.13572	1.89491×10^{4}	0.99721
Cycle 4	8.31665	0.03483	1.50264×10^{5}	0.99657	3.70724	0.09405	1.55857×10^{4}	0.99860
Cycle 5	11.18406	0.01837	1.11452×10^{5}	0.99729	10.86676	0.18112	1.59953×10^{4}	0.99972
Cycle 6	7.72655	0.03759	7.61056×10^{6}	0.99713	2.51254	0.01347	2.35983×10^{4}	0.99899
Cycle 7	19.36415	0.00476	1.34925×10^{5}	0.99306	10.46316	0.07656	1.56675×10^{4}	0.99869

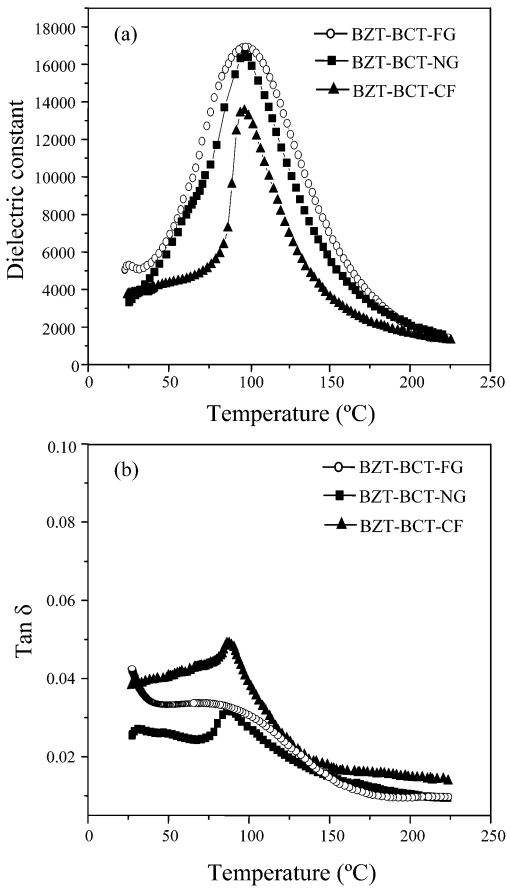

Fig. 8 Temperature dependences of (a) dielectric constant (ε_r) and (b) dielectric loss (tan δ) values within the range 25 225 °C at constant frequency of 10 kHz measured for prepared BZT BCT ceramics sintered at 1350 °C.

values measured for BZT–BCT-NG ($\varepsilon_r \sim 3557$) and BZT–BCT-CF ($\varepsilon_r \sim 3409$). The tan δ *versus* T plots (Fig. 8(b)) show a small loss (tan δ values) for BZT–BCT-FG ceramics along the entire temperature range tested. The values of ε_r and tan δ obtained for various BZT–BCT sintered ceramics are illustrated in Table 4. The higher ε_r value measured for BZT–BCT-FG can be attributed to the enhanced homogeneity of BZT–BCT ceramics derived from the FG powder as a result of the higher compaction degree of the green bodies and their better sintering ability in

Table 4 Measured dielectric constant and dielectric loss (tan δ) values for various BZT BCT ceramics sintered at 1350 °C

Samples	ε_r	tan δ
BZT BCT NG	3557	0.027
BZT BCT FG	4984	0.035
BZT BCT CF	3409	0.037

comparison with those derived from the NG BZT–BCT powder. It can be concluded that the treatment of the powder strongly affects the dielectric properties, not only the losses that would be expected, but also the real part. If not treated, as in the case of the BZT–BCT-CF ceramic, only one phase transition in dielectric responses at higher T_c can be found with higher loss values in comparison with those of FG ones, revealing the efficacy of treatment.

Fig. 9 shows the frequency dispersion of real (ε') and imaginary (ε'') parts of dielectric constant values of BZT–BCT ceramics prepared at different conditions in the range from 100 Hz to 1 MHz. For all samples, the ε' and ε'' values decrease with increasing frequency, a commonly observed behavior for dielectric/ferroelectric materials. The fall in dielectric constant arises because polarization does not occur instantaneously with application of the electric field as charges possess inertia. The delay in the response towards the impressed alternating electric field at high frequencies leads to loss and thus, decline in dielectric constant. Higher values of ε' were measured for BZT–BCT-FG compared with BZT–BCT-NG ceramics in all frequency ranges tested, which could be attributed to the resulting high dense ceramic on sintering of BZT–BCT-FG material. The high ε_r values associated with the low tan δ values (Fig. 8) lead to lower values of ε'' for BZT–BCT-FG ceramics when compared with ε'' values measured for BZT–BCT-NG ceramics, as shown in Fig. 9. For BZT–BCT-NG ceramics, the decrease in grain size and the concomitant increase in the number of grain boundaries resulted in lower polarization intensity, and therefore, in lower ε_r values.[30] A Cole–Cole plot for the prepared samples is shown in the inset to Fig. 9. The Cole–Cole equation for complex permittivity can be written as:

$$\varepsilon^* = \varepsilon' + i\varepsilon'' = \varepsilon_\infty + \frac{\varepsilon_s \quad \varepsilon_\infty}{1 + (i\omega\tau)^{1-\alpha}} \quad i\frac{\sigma_{dc}}{\varepsilon_0\omega} \qquad (14)$$

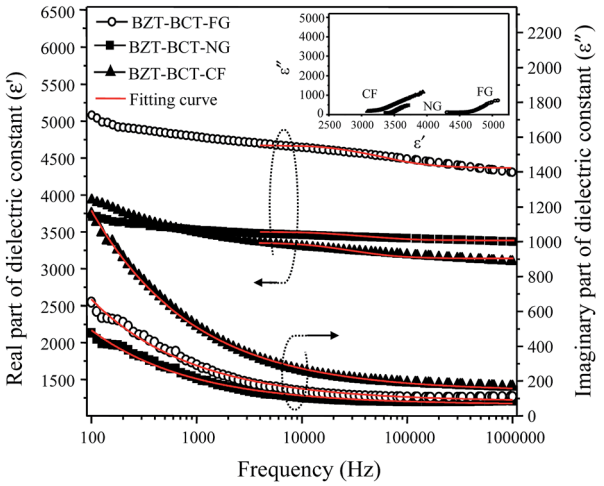

Fig. 9 Real (ε') and imaginary (ε'') parts of dielectric constant values of BZT BCT ceramics in the frequency range from 100 Hz to 1 MHz measured for various BZT BCT ceramics sintered at 1350 °C. Inset shows corresponding Cole Cole plot.

Table 5 Various fitting parameters obtained from fitting frequency dispersion behavior of real and imaginary parts of the dielectric constant (Fig. 9)

Samples	ε_∞	ε_s	τ	n
BZT BCT NG	3386.637	3462.918	2.83×10^{-6}	0.54014
BZT BCT FG	4359.056	4643.406	1.95×10^{-6}	0.54714
BZT BCT CF	3132.525	3318.082	3.45×10^{-6}	0.54962

where: ε_s and ε_∞ are the dielectric constants on the low and high frequency sides of the relaxation, ω is the angular frequency ($\omega = 2\pi f$), τ is the relaxation time, and α indicates the width of the relaxation time distribution and provides a measure of the polydispersive nature. The second term in the equation is a result of high conducting behavior contributing only to ε''. Assuming a single relaxation time τ, the variation of ε_r with ω is given by the Debye equation as:

$$(\varepsilon_r \quad \varepsilon_\infty)/(\varepsilon_s \quad \varepsilon_\infty) = (1 \quad j\omega\pi)/(1 + \omega^2\tau^2), \tag{15}$$

This gives the relation for ε' and ε'' at high frequency as[31]

$$\varepsilon' = \varepsilon_\infty + (\varepsilon_s \quad \varepsilon_\infty)/(1 + 4\pi^2 f^2\tau^2), \tag{16}$$

$$\varepsilon'' = 2\pi f\tau(\varepsilon_s \quad \varepsilon_\infty)/(1 + 4\pi^2 f^2\tau^2) \tag{17}$$

The associated dielectric parameters, ε_∞, ε_s and τ were evaluated by fitting ε' *versus* frequency variation in the high frequency region with eqn (16) as shown in Fig. 9. The various fitting parameters are listed in Table 5. An increase in the value of ε_∞ (4359.056) as well as ε_s (4643.406) for BZT–BCT-FG ceramic was observed when compared with corresponding values measured for BZT–BCT-NG ceramic (ε_∞ = 3386.63; ε_s = 3462.918). Furthermore, the measured values are even lower for the BZT–BCT-CF sample, meaning that besides granulation, the surface treatment also matters. This is an obvious consequence of stoichiometric deviations caused by hydrolysis occurring during the aging period in water in the case of non-surface treated samples. The variation of ε'' with frequency at room temperature was fitted with the power equation given by Jonscher, as $\varepsilon'' \propto f^{n-1}$, where, $0 \leq n \leq 1$.[32] The values of exponent n, obtained after fitting as shown in Fig. 9, are also listed in Table 5. A slight increase in the exponent n was found for the BZT–BCT-FG ceramic when compared with BZT–BCT-NG. It has been suggested[33] that further improvements on dielectric loss of BZT–BCT ceramics could be obtained by adding MgO and Al_2O_3 as additives. Furthermore, varying the Zr/Ti and Ba/Ca ratios in the solid solution has also been highlighted as a way for tailoring the dielectric constant for tunable capacitor applications.[33]

D Conclusions

Micro-sized granules of lead free BZT–BCT piezoelectric material *via* a freeze granulation method were successfully fabricated *via* spraying a stable aqueous suspension into liquid nitrogen (freeze granulation), followed by freeze-drying. From the results obtained it can be concluded that freeze granulation enhances the packing ability of the powder and achieves higher levels of green density and homogeneity in green compacts, features that improve the sintering ability and the overall properties of sintered ceramics. The consistency of functional properties such as phase transition temperatures of BZT–BCT-FG ceramics with those of BZT–BCT-NG ceramics showed that the material is not negatively affected by the surface treatment applied to the BZT–BCT powder to protect it against hydrolysis. The results also showed that aqueous processing of non-surface treated BZT–BCT powder leads to formation of impurity phases derived from non-stoichiometric, cationic leaching when the powder is dispersed in water. These hydrolysis reactions degrade the functional properties of the resultant BZT–BCT ceramics.

Acknowledgements

The Authors, Ajay Kaushal, S. M. Olhero, Budhendra Singh, Reza Zamiri and V. Saravanan would like to thank the Foundation for Science and Technology of Portugal (FCT) for the financial support under the grant references SFRH/BPD/77598/2011, SFRH/BPD/87486/2012, SFRH/BPD/76184/2011, SFRH/BPD/76185/2011 and SFRH/BPD/80742/2011, respectively. The authors would also like to thank CICECO for the work at the University of Aveiro and FCT for the financial support under the project PTDC/CTM/099489/2008.

Notes and references

1 A. Neubrand, R. Lindner and P. Hoffmann, *J. Am. Ceram. Soc.*, 2000, **83**(4), 860.
2 J. M. F. Ferreira, S. M. Olhero and A. Kaushal, *J. Eur. Ceram. Soc.*, 2013, **33**, 2509.
3 W. Liu and X. Ren, *Phys. Rev. Lett.*, 2009, **103**, 257602.

4 W. Yugong, H. Zhang, Y. Zhang, M. Jinyi and X. Daohua, *J. Mater. Sci.*, 2003, **38**, 987.
5 T. Takenaka and H. Nagata, *J. Eur. Ceram. Soc.*, 2005, **25**, 2693.
6 V. S. Puli, A. Kumar, D. B. Chrisey, M. Tomozawa, J. F. Scott and R. S. Katiyar, *J. Phys. D: Appl. Phys.*, 2011, **44**, 395403.
7 V. S. Puli, D. K. Pradhan, W. Pérez and R. S. Katiyar, *J. Phys. Chem. Solids*, 2013, **74**, 466.
8 P. Mishra, Sonia and P. Kumar, *J. Alloys Compd.*, 2012, **545**, 210.
9 H. Bao, C. Zhou, D. Xue, J. Gao and X. Ren, *J. Phys. D: Appl. Phys.*, 2010, **43**, 465401.
10 S. Su, R. Zuo, S. Lu, Z. Xu, X. Wang and L. Li, *Curr. Appl. Phys.*, 2011, **11**, S120.
11 B. Li, J. E. Blendell and K. J. Bowman, *J. Am. Ceram. Soc.*, 2011, **94**, 3192.
12 D. A. Anderson, J. H. Adair, D. Miller, J. V. Biggers and T. R. Shrout, Surface Chemistry Effects on Ceramic Processing of $BaTiO_3$ Powder, in *Ceramic Transactions, Ceramic Powder Science II*, G. L. Messing, E. K. Fuller Jr and H. Hausner, Am. Ceram. Soc., Westerville, OH, 1988, vol. 1, pp. 485–492.
13 P. Nanni, M. Leoni, V. Buscaglia and G. Aliprandi, *J. Eur. Ceram. Soc.*, 1994, **14**, 85.
14 H. W. Nesbitt, G. M. Bancroft, W. S. Fyfe, S. N. Karkhanis and A. Nishijima, *Nature*, 1981, **289**, 358.
15 S. M. Olhero, I. Ganesh, P. M. Torres and J. M. F. Ferreira, *Langmuir*, 2008, **24**, 9525.
16 S. M. Olhero, I. Ganesh, P. M. C. Torres, F. L. Alves and J. M. F. Ferreira, *J. Am. Ceram. Soc.*, 2009, **92**, 9–16.
17 A. Kaushal, S. M. Olhero and J. M. F. Ferreira, *J. Mater. Chem. C*, 2013, **1**, 4846.
18 S. Mahajan, O. P. Thakur, D. K. Bhattacharya and K. Sreenivas, *Mater. Chem. Phys.*, 2008, **112**, 858.
19 B. Nyberg, E. Carlstrom and R. Carlsson, Freeze granulation of liquid phase sintered silicon carbide, in *Ceramic transaction, Silicon-Based Structural Ceramics*, W. Brian Sheldon and Stephen C. Denforth, American Ceramic Society, Westerville, Ohio, 1994, vol. 42, pp. 107–113.
20 H. A. Janssen, *VDI Z.*, 1895, **39**, 1045.
21 *Joint Committee on Powder Diffraction Standards* (JCPDS) card no. 05-0626.
22 M. F. C. Ladd and R. A. Palmer, *Structure Determination by X-ray Crystallography*, 3rd edn, Plenum Press, New York, 1993.
23 B. D. Cullity and S. R. Stock, *Elements of X-Ray Diffraction*, third edn, Prentice Hall, New Jersey, 2001.
24 J. t. Langford and A. Wilson, *J. Appl. Crystallogr.*, 1978, **11**(2), 102.
25 A. Kaushal, S. M. Olhero, P. Antunes, A. Ramalho and J. M. F. Ferreira, *Mater. Res. Bull.*, 2014, **50**, 329.
26 J. Zheng and J. S. Reed, *J. Am. Ceram. Soc.*, 1988, **71**(11), C456.
27 W. C. Oliver and G. M. Pharr, *J. Mater. Res.*, 2004, **19**, 3.
28 J. H. Gong, J. J. Wu and Z. D. Guan, *J. Eur. Ceram. Soc.*, 1999, **19**, 2625.
29 E. Tasarkuyu, A. Coskun, A. E. Irmark, S. Akturk, G. Unlu, Y. Samancioglu, A. Yucel, C. Sarikurkcu, S. Aksoy and M. Acet, *J. Alloys Compd.*, 2011, **509**, 3717.
30 F. Yan, P. Bao, H. L. W. Chan, C. L. Choy and Y. Wang, *Thin Solid Films*, 2002, **406**, 282.
31 M. Davies, *Some electrical and optical aspects of molecular behaviour*, Pergamon Press, London, 1965, vol. 337.
32 A. K. Jonscher, *Dielectric Relaxation in Solids*, Chelsea Dielectrics press, London, 1983.
33 X. G. Tang and H. L. W. Chan, *J. Appl. Phys.*, 2005, **97**, 034109.